Desalination and Water Treatment
www.deswater.com

doi: 10.5004/dwt.2023.29961

312 (2023) 79–88
November

Improvement of photocatalysis using ZnO/zeolite nanocomposites for contaminant removal in aqueous media

Fanny Servín de Dios, Erik Ramírez Morales, Marcela del Carmen Arellano Cortaza, Germán Pérez Hernández, Erika Viviana Miranda Mandujano, Edicson Macedonio López Alejandro, Lizeth Rojas Blanco*

Universidad Juárez Autónoma de Tabasco, Avenida Universidad S/N, Col. Magisterial, Villahermosa, Tabasco. CP. 86040 México, Phone: +52-993-246-8500; email: lizethrb@gmail.com (L.R. Blanco), Phone: +52-554-924-5211; email: fannysd1@gmail.com (F.S. de Dios), Phone: +52-777-152-8063; email: erik.ramirez@ujat.mx (E.R. Morales), Phone: +52-914-125-7385; email: marcela.arellano@ujat.mx (M. del Carmen Arellano Cortaza), Phone: +52-933-168-3941; email: gph08@hotmail.com (G.P. Hernández), Phone: +52-777-134-0605; email: erika.miranda@ujat.mx (E.V.M. Mandujano), Phone: +52-993-297-6215; email: edicsonmlop@gmail.com (E.M.L. Alejandro)

Received 29 March 2023; Accepted 7 September 2023

ABSTRACT

In order to take advantage of the adsorbent capacity of zeolites, in the present work, ZnO particles and ZnO/zeolite nanocomposites were synthesized, using a natural zeolite and a synthetic zeolite structure. Compounds of: ZnO, ZnO/CLI (CLI = clinoptilolite zeolite) and ZnO/NaA (NaA = sodium type A zeolite) were synthesized by the sol–gel method and physical milling. The structural, morphological, textural and optical properties of the materials were characterized by X-ray diffraction, scanning electron microscopy and transmission electron microscopy, N_2 physisorption and UV-Vis spectroscopy. Nanocomposites with crystallite sizes between 20–30 nm were obtained. The morphology presents grains distributed in the composites, while agglomerates are observed in pure ZnO. The ZnO surface area decreases slightly in the CLI composite but in the ZnO/NaA composites the decrease is notable. The band gap of the materials is between 3.18–3.21 eV. Photocatalytic activity was evaluated using aqueous solutions of organic dyes such as methylene blue and rhodamine B at initial concentrations of 10 and 20 mg·L^{-1}. The photocatalytic performance increased ~60%, which shows that the use of semiconductor oxides supported on zeolites is a viable and efficient process in the reduction of contaminants present in wastewater.

Keywords: Zinc oxide; Clinoptilolite; NaA; Semiconductors; Aluminosilicates

1. Introduction

Water contamination by agents such as solid waste, hydrocarbons, pesticides, dyes, etc., is a serious problem since it causes water scarcity, diseases, and environmental deterioration [1].

Dyes are widely used substances in various industries, such as food, textiles, and paints. However, the mismanagement of waste brings with it enormous environmental problems, so the removal of these pollutants remains a challenge. Until now, conventional methods for the treatment of wastewater have not shown the desired efficacy, since in most cases the treated dyes generate dangerous by-products, such as aromatic amines [2].

Methylene blue (MB, $C_{16}H_{18}ClN_3S$), also known as methyl bromide, belongs to the family of cationic dyes and

* Corresponding author.

is used for various applications in both the textile and pharmaceutical industries [3]. The presence of this dye in bodies of water brings with it various effects not only on the flora and fauna of the environment but also on human health because it could cause problems both in the respiratory tract and the skin [4].

On the other hand, rhodamines are a class of dyes used in various applications in the paper, textile, cosmetic, and pharmaceutical industries. For example, these molecules are used as biomarkers, photosensitizers, flow cytometry, ELISA tests, etc., due to their optical properties [5]. Rhodamine B (RhB, $C_{28}H_{31}ClN_2O_3$) generates irritation to the skin, eyes, digestive tract, and respiratory system, in addition, the by-products generated from partial degradation due to inadequate waste treatment of this contaminant can become mutagenic. and carcinogens [6]. So, the elimination of this type of contaminant represents a challenge for nanomaterials used in wastewater treatment.

Among the alternatives that have been used to resolve or delay the effects of water pollution are filtration [7], adsorption [8], oxidation [9,10], flocculation [11], and photocatalysis [12,13], among others. Photocatalysis is an effective alternative that achieves the removal of organic contaminants [14], using the hydroxyl radicals generated when the photocatalyst is exposed to a radiation source [15,16]. Some photocatalytic semiconductors are Al_2O_3 [17], ZnO [18], Fe_2O_3 [19], CeO_2 [20], TiO_2 [21], $FeWO_4$ [22], ZnSe [23], Cu_2O [24], etc.

ZnO is an n-type semiconductor, which has been of interest due to its availability, oxidation capacity, and low toxicity [25]. However, ZnO has disadvantages such as low surface area, tendency to form agglomerates, high recombination rate of electron/hole pairs, and low adsorption capacity [26,27]. Due to the limitations in photocatalytic applications of ZnO, alternatives have been investigated that allow increasing the generation of hydroxyl radicals, increasing their range of absorption of ultraviolet and visible light, and their adsorption capacity. Improvements have been obtained by doping semiconductor materials, synthesizing nanocomposites [28], or using porous supports [29,30]. The development of this type of catalyst has aroused the interest of the scientific community, because it presents excellent properties, which make it a promising material, for example, efficient rate of degradation of organic contaminants, good photostability, and relatively simple synthesis [31,32].

The formation of nanocomposites is very useful in the field of photocatalysis, since in addition to increasing the range of light absorption, in the UV and visible range, the recombination effects of the e^-/h^+ pair are avoided or diminished thus increasing the charge separation and increasing the specific surface area about bare semiconductor, etc. [33].

In this way, zeolites are materials that have a porous structure, large specific surface area, good thermal and chemical stability, and a high affinity for contaminating molecules, which can achieve the improvement of semiconductors, such as ZnO [34,35].

Zeolites are aluminosilicates with a microporous structure, a high adsorption capacity, capable of reversibly hydrating and dehydrating, and a high ion exchange potential [36]. Zeolites are present in two types, natural ones, which are present in deposits and have great abundance, and synthetic ones, which are designed in the laboratory to simulate the conditions and structures of natural ones [37,38]. Therefore, the use of zeolites as metal oxide support is the best way to prepare hybrid catalysts, which will disperse in an orderly manner and can be effectively separated from the reaction system.

In the present work, ZnO particles and ZnO/zeolite nanocomposites were synthesized, in which a natural zeolite and a synthetic zeolite structure were used. The structural, morphological and optical properties of ZnO/zeolite nanocomposites are analyzed, as well as their photocatalytic behavior in ultraviolet light. In addition, zeolite is evaluated as a highly viable support due to its suitable channels for application in photocatalysis.

2. Experimental set-up

2.1. Materials

For the synthesis of the materials, $Zn(C_2H_3O_2)_2{\cdot}2H_2O$ (98%, Sigma-Aldrich), C_2H_5OH (99.5%, MEYER), NaOH (97%, CiveQ) y H_2O were used. MB ($C_{16}H_{18}N_3SCl$, 98.5%, CiveQ) and rhodamine B (RhB) ($C_{28}H_{31}N_2O_3Cl$, 99%, MEYER). The natural zeolite used was calcium clinoptilolite from El Cajón, Sonora, Mexico, sieved through #360 mesh, and type A sodium zeolite was used as synthetic zeolite (Sigma-Aldrich).

2.2. ZnO synthesis

ZnO particles were prepared using the sol–gel method described by Torres-Hernández et al. [39], using forced hydrolysis of $Zn(C_2H_3O_2)_2{\cdot}2H_2O$, NaOH, and a small percentage of distilled water with absolute ethanol as a solvent, to obtain ZnO particles with controlled size. The synthesis process was divided into two stages: the first consists in forming the nuclei of the ZnO particles and in the second stage their growth.

In the first stage, 117.2 mg NaOH was dispersed in 10 mL of ethanol, this solution was sonicated for 10 min and then 20 min at 50°C, of which 965 μL were poured into 35.825 mL of ethanol. This solution was prepared with 339.3 mg of $Zn(C_2H_3O_2)_2{\cdot}2H_2O$ in 45 mL of ethanol. The suspension was kept stirred for 5 h and at a temperature of 50°C. In stage two, a solution with 5 times the initial weight of $Zn(C_2H_3O_2)_2{\cdot}2H_2O$ in 3.3 mL of H_2O was added at 40°C, then a solution with 5 times the initial weight of NaOH in 3.5 mL of H_2O at 40°C, to finally carry out the dispersion of ZnO in ethanol-water.

This solution was kept stirring at a temperature of 50°C for 1 h, then it was left to rest for 24 h, at the end of this time it was decanted to obtain the ZnO precipitate washed with deionized water and dried at 120°C for 12 h.

2.3. Synthesis of ZnO/CLI and ZnO/NaA

The synthesis used for the composites was like that reported [40]. The ZnO and the natural and synthetic zeolites were ground in a mortar for 30 min, using C_2H_5OH as the control agent. The proportion was 30% by weight of ZnO concerning the weight of the zeolites. The composites were dried for 2 h at 60°C.

2.4. Characterization

For X-ray diffraction, a Bruker D2 phaser diffractometer was used, with Cu Kα radiation of λ = 1.5418 Å, in a 2θ range of 10°–80°, speed 4°/min. For morphology, a Tescan Mira 3 microscope was used, at a voltage of 20 kV. High-resolution transmission electron microscopy (HRTEM) images were taken at 200 kV with a JEOL JEM-2100. UV-Vis spectra were obtained with a Perkin Elmer Lambda 9 model spectrophotometer with an integrating sphere. Physisorption of N_2 was carried out in Autosorb iQ Station 1 equipment.

2.5. Photocatalytic evaluation

For the photocatalytic tests, 12 mg of photocatalyst was used in 80 mL of contaminant solution (10 and 20 mg·L^{-1}). The resulting solution was stirred in the dark for 40 min (adsorption–desorption equilibrium). After that, the solution was irradiated with an ultraviolet light lamp with an irradiance of 95 W·m^{-2} and a power of 20 W. The photocatalytic degradation efficiency was calculated using Eq. (1):

$$\%\text{Deg} = \frac{C_0 - C_e}{C_0} \times 100 = \frac{A_0 - A_t}{A_0} \times 100 \quad (1)$$

where C_0 is the initial concentration of the dye and C_t is the concentration of the dye at time t [41].

3. Results and discussion

3.1. X-ray diffraction

The diffraction patterns of the pure materials and the composites are shown in Fig. 1a. In the ZnO diffractogram, a hexagonal wurtzite structure is observed. The characteristic reflections are found at positions 2θ = 31.63°, 34.29°, 36.13°, 47.40°, 56.44°, 62.70°, 66.19°, 67.79° and 68.97° (PDF No. 36-1451) [26]. The natural zeolite sample, clinoptilolite (CLI) shows the following peaks: (200),$(20\bar{1})$, (111), $(13\bar{1})$, (400),$(22\bar{2})$, $(42\bar{2})$, (151) and (530) correspond to the positions 2θ = 11.13°, 13.02°, 17.31°, 19.06°, 22.40°, 26.01°, 28.10°, 30.11° and 31.93°, respectively (PDF No. 39-1383), associated with calcium clinoptilolite with a monoclinic structure [42]. The ZnO/CLI sample shows peaks associated with the hexagonal wurtzite phase and the calcium clinoptilolite structure. The synthetic zeolite type NaA sample (NaA) exhibited peaks at 2θ = 12.37°, 16.04°, 21.59°, 23.92°, 27.05°, 29.88° and 34.10°, which are associated with a zeolite with a cubic structure (PDF No. 39-0222) [43]. In the ZnO/NaA sample, the hexagonal wurtzite phase of ZnO and the cubic structure of NaA are present, the amplitude of this signal is increased due to the overlapping of signals in the (002) plane of ZnO with the (664) plane of the NaA.

In the diffractograms of ZnO/zeolite composites Fig. 1b, a decrease and a shift position in the ZnO peaks are observed

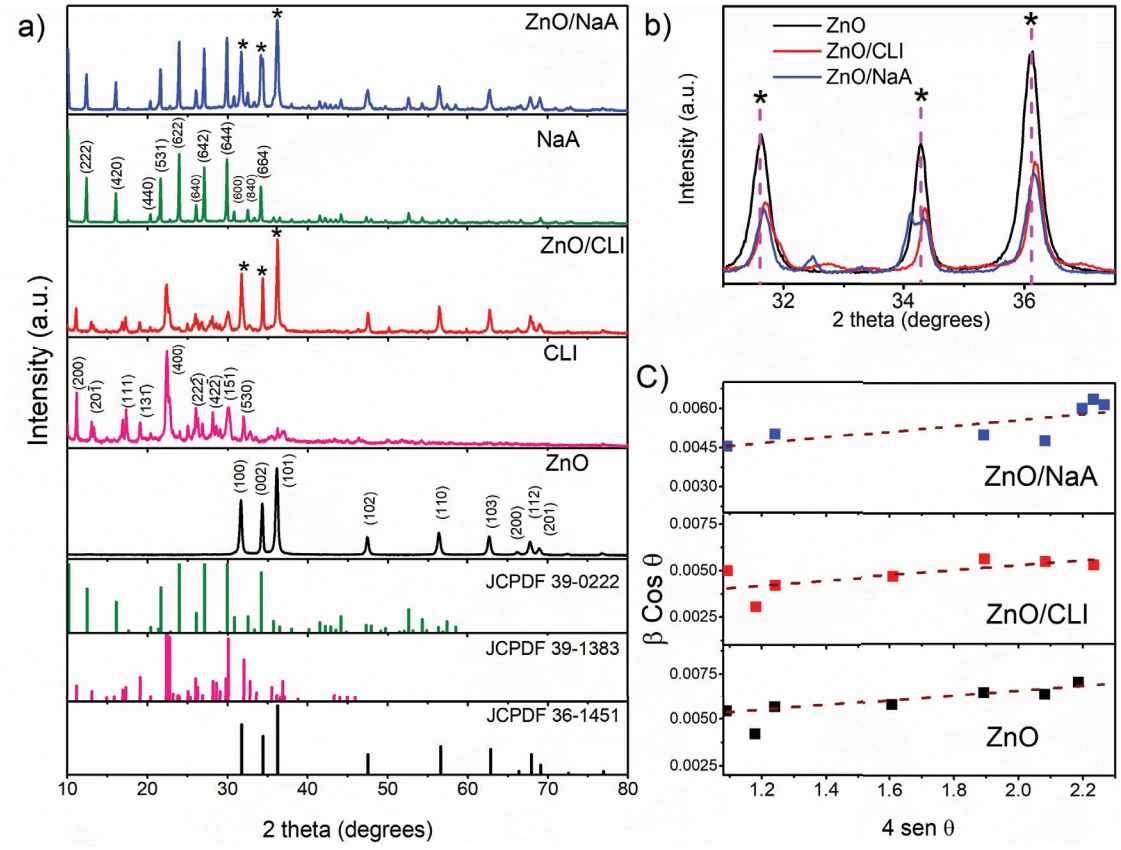

Fig. 1. (a) X-ray diffraction patterns of pure ZnO, CLI, NaA, ZnO/CLI, and ZnO/NaA. The symbol * represents the main signs of ZnO. (b) planes (100), (002) and, (101) of ZnO, ZnO/CLI and ZnO/NaA. (c) 4 sinθ vs. β cosθ plots using Williamson–Hall uniform deformation model analysis of the ZnO, ZnO/CLI and ZnO/NaA nanocomposites.

when the material is supported on the zeolite, which is associated with the low ZnO charge and the overlapping of its peaks with those of the zeolites [44]. This indicates that the ZnO particles preferentially remain outside the zeolitic structure [45]. Signals associated with impurities are not observed in any of the samples.

Average crystallite size and lattice strain in the samples were estimated utilizing the uniform deformation model of the Williamson–Hall, utilizing the relation [46]:

$$\beta\cos\theta = \frac{K\lambda}{D} + 4\varepsilon\sin\theta \quad (2)$$

where K is a shape factor, which is ~0.9 for spherical particles, ε is the lattice strain, β is the full width at half maximum (FWHM) of the considered diffraction peak in radian, θ is the Bragg's angle, λ is the X-ray wavelength, and D is the crystallite size. Using the slope and the intercept in the ordinate axis of the linear fits of the βcosθ vs. 4sinθ plots, lattice strain and average crystallite sizes in the samples were estimated, respectively (Fig. 1c) [47]. The results are summarized in Table 1.

The lattice parameters in the composites were calculated individually to identify the distortions of the pure and composite materials. The calculated parameters are shown in Table 1, the observed variations are associated with the incorporation of the ZnO particles to the respective supports used, as well as the synthesis method (milling).

3.2. Scanning electron microscopy

The morphology of the ZnO particles exhibited flake-like grains, the formation of conglomerates is observed (Fig. 2a), associated with the precursors used in the synthesis and the CLI sample (Fig. 2b) presented irregular agglomerates in the shape of flakes [48]. The micrographs of the ZnO/CLI composite (Fig. 2c) show a combination of the two previous morphologies and a dispersion of the particles is observed, which improves the photocatalytic activity, since the high agglomeration decreases the surface area [49,50]. On the other hand, in the NaA sample, cubic forms with well-defined smooth faces are observed (Fig. 2d). For the ZnO/NaA sample, smaller particles, attributed to ZnO, are observed on the faces of the zeolite NaA cubes (Fig. 2e). ZnO on the zeolite does not modify the morphology, which corroborates the X-ray diffraction (XRD) results [51].

3.3. High-resolution transmission electron microscopy

In Fig. 3a, hexagonal shapes are observed for the ZnO sample. In Fig. 3d and f, the light-colored forms are associated with zeolites and the dispersed dark particles are related to ZnO. In the elemental mapping analysis (Fig. 3g),

Table 1
Crystallite size and lattice parameters of ZnO of pure materials and composites

Sample	Av. crystallite size (nm)	Lattice parameters		Strain
		a (Å)	*c* (Å)	ε
ZnO	36	3.26968	5.23908	0.00132
ZnO/CLI	52	3.26286	5.22736	0.00129
ZnO/NaA	42	3.26554	5.23200	0.00115

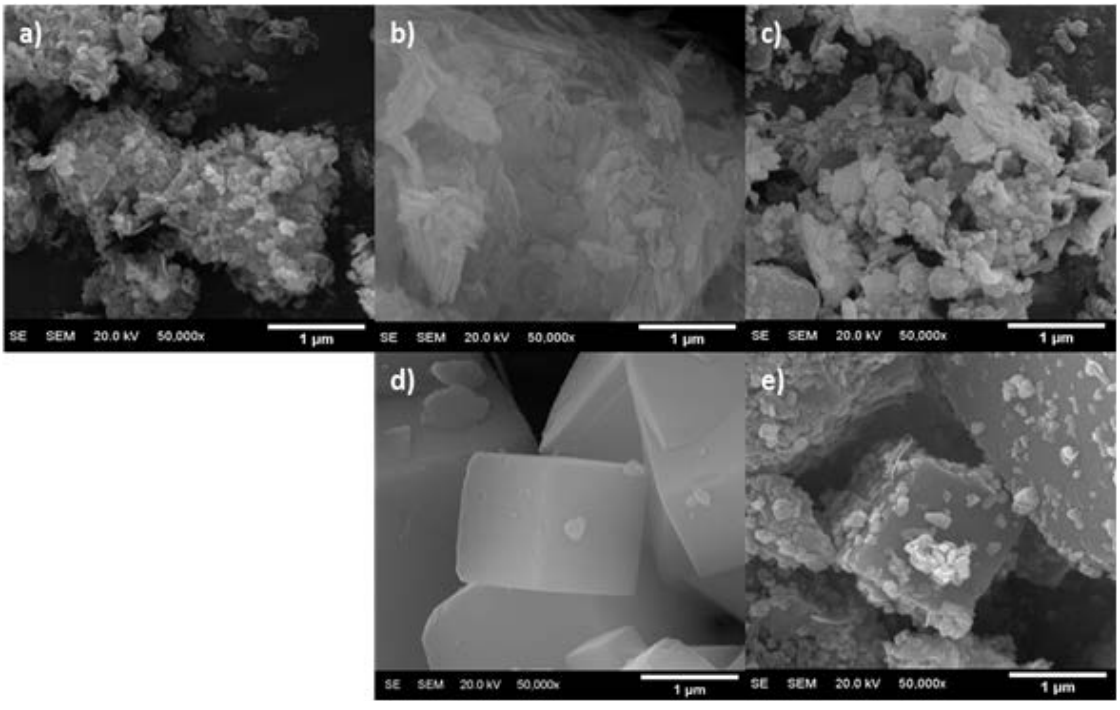

Fig. 2. Scanning electron microscopy micrographs with 50,000x magnification of samples (a) ZnO, (b) CLI, (c) ZnO/CLI, (d) NaA and (e) ZnO/NaA.

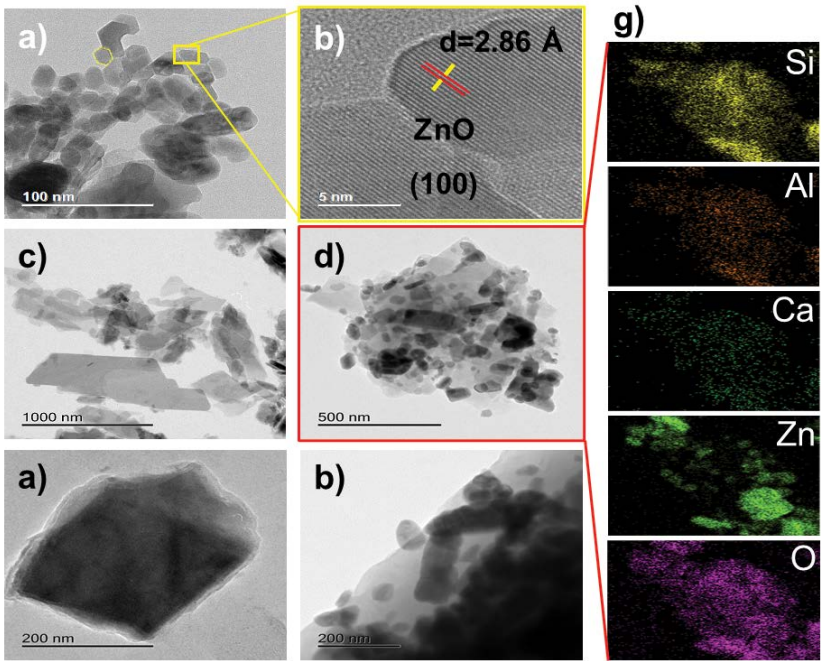

Fig. 3. Transmission electron microscopy micrographs of (a) ZnO, (c) CLI, (d) ZnO/CLI, (e) NaA and (f) ZnO/NaA. (b) HRTEM image of ZnO. (g) Energy-dispersive X-ray spectroscopy analysis of ZnO/CLI.

the presence of Si, Al, Ca, Zn and O is identified. The mapping shows that the clinoptilolite contains more Si than Al. The darkest areas are mostly Zn, which eliminates the existence of Zn^{2+} substitutions in the CLI crystal lattice. It is also observed that O is dispersed in the sample, which could be due to the presence of by-products in the synthesis such as SiO_4 and AlO_4.

On the other hand, results by HRTEM (Fig. 3b), reveal the crystallinity of ZnO, the interplanar distance of 2.86 Å is attributed to the crystal plane (100) of the wurtzite hexagonal structure of ZnO [52], which agrees with a value obtained by XRD of ~2.83 Å for the same plane. This analysis could not be performed on zeolites due to charge accumulation on this material [53].

3.4. UV-Vis

Fig. 4 shows the absorbance spectra of ZnO, ZnO/CLI, and ZnO/NaA, showing an absorption edge at 395, 388, and 392 nm, respectively. The similarity in the edges of ZnO and ZnO/NaA can be attributed to the good distribution of ZnO on the zeolitic structure [54]. The slight shift in the absorption edge of the ZnO/CLI spectrum is associated with a decrease in the recombination of electron/hole pairs, which causes an increase in the band gap [55]. In addition, ZnO/CLI exhibits an increase in absorbance in the visible region, attributed to the O vacancies of ZnO by incorporation into the clinoptilolite structure [56].

The bandgap (Inset Fig. 4) was calculated using the Kubelka–Munk equation [27]:

$$F(R) = \frac{(1-R)^2}{2R} \tag{3}$$

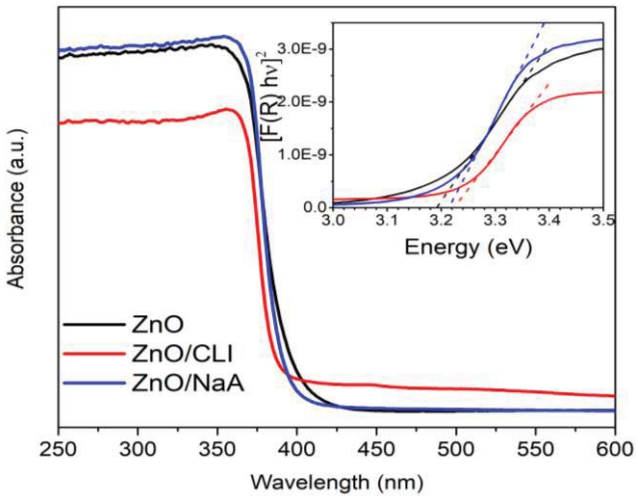

Fig. 4. Absorbance spectrum of ZnO, ZnO/CLI and ZnO/NaA. Energy gap calculation using the Kubelka–Munk method (inset).

where R is the absolute value of the reflectance. The bandgap values obtained are 3.18, 3.23 and 3.21 eV for ZnO, ZnO/CLI and ZnO/NaA, respectively. The increase in the energy gap is attributed to the variation in the ZnO particle size and the detection on the surface of the zeolites [57]. The increase in the band gap in the composites is also attributed to the fact that zeolites are non-conductive materials; when these are combined with low percentages of semiconductor materials, it is possible that the value of the bandgap increases. An alternative to reduce the value would be increasing the amount of ZnO supported on the porous material.

3.5. Physisorption of N_2

Fig. 5 shows the samples with type IV isotherms for mesoporous materials [58] which is attributed to the secondary porosity of the zeolites. The conjugation of mesopores and micropores allows larger molecules to be adsorbed, which is favorable for photocatalytic applications [59]. The hysteresis loop is of the H_3 type, formed at relative pressures (P/P_0) > 0.5, and is associated with slit-shaped mesopores [60]. Synthetic zeolite shows type H_4 hysteresis attributed to narrow pore sizes [61].

The specific surface area of CLI decreases when ZnO is supported (Table 2), which is associated with pore narrowing and sedimentation [60]. In contrast, the surface area of NaA increased when ZnO was supported, which is attributed to the formation of a porous layer on the zeolite surface [43]. The distribution of pore sizes is observed in the inserts of Fig. 6, in which the main peak is found at the limit of the micropores and mesopores for ZnO and zeolites. In the ZnO/zeolite composites, the pore size distribution is bimodal, with peaks centered at ~3 and 32 nm, confirming the presence of mesopores.

Table 2
Textural properties obtained by adsorption–desorption of N_2

Sample	Superficial area BET ($m^2 \cdot g^{-1}$)	Pore volume BJH ($cm^3 \cdot g^{-1}$)	Pore diameter BJH (nm)
ZnO	22.72	0.155	3.83
CLI	23.38	0.135	3.83
ZnO/CLI	17.01	0.172	3.83
NaA	0.99	0.003	3.40
ZnO/NaA	3.92	0.033	3.83

3.6. Preliminary adsorption evaluation

The adsorption and photocatalysis of CLI and NaA zeolites in MB at 20 $mg \cdot L^{-1}$ with 12 mg of sample were evaluated

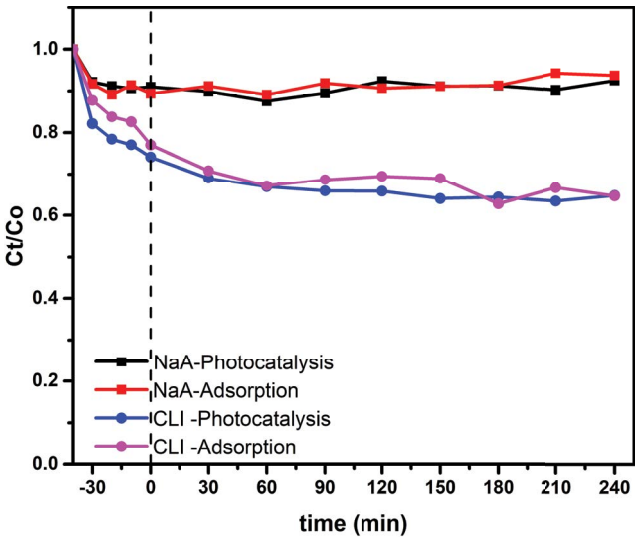

Fig. 6. Adsorption and photocatalysis for CLI and NaA.

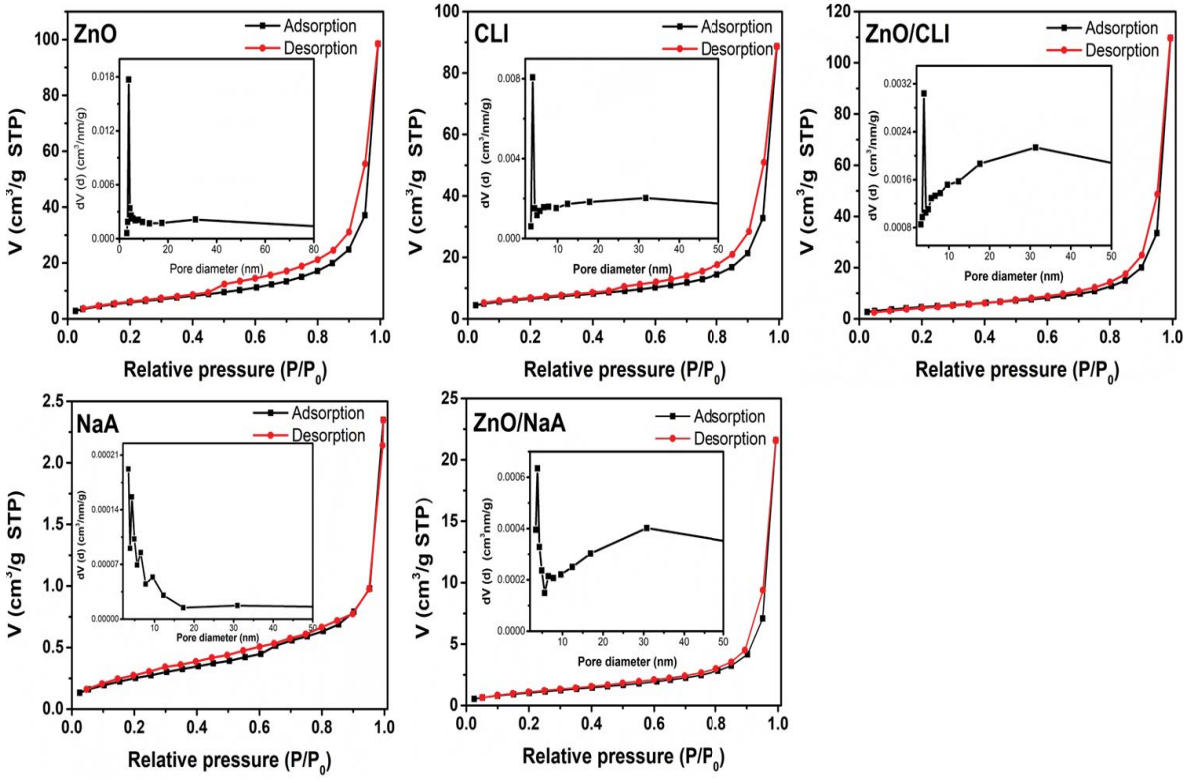

Fig. 5. Adsorption–desorption isotherms of N_2 at 77.35 K of the study samples. Insert: pore-size distribution.

(Fig. 6). The processes are similar in the two types of zeolites, there is no degradation activity under photonic radiation, they only adsorb [62]. CLI showed higher adsorption capacity than NaA, which is influenced by electrostatic attraction between the negatively charged surface of zeolites and the charge of MB (cationic) [63].

3.7. Effect of ZnO loading on zeolite

Three loading percentages (5%, 10% and 30% by weight) of ZnO on NaA were evaluated. The effect on the synthetic zeolite was evaluated, due to the low adsorption it showed, which allows the photocatalytic activity to be gradually evaluated. In this work, a load of 30% by weight was established. Is shown in Fig. 7 that the increase in the percentage of ZnO causes an increase in photocatalytic degradation, which is associated with the increase in active sites available for the contaminant [64]. However, a percentage close to the optimal value reduces the number of photons that reach the inner layers of the photocatalyst, also causes

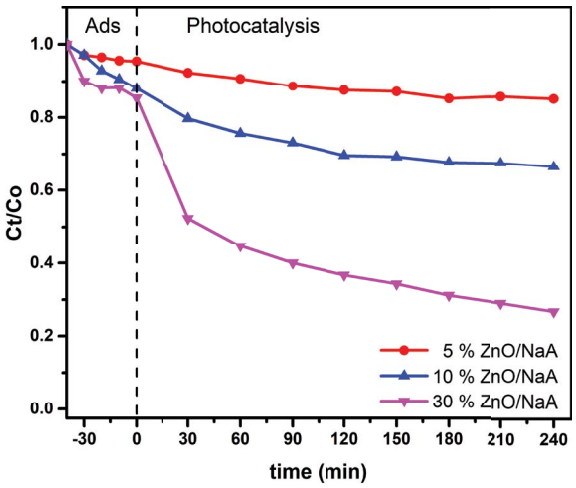

Fig. 7. Evaluation of the effect of ZnO loading on zeolite NaA, in Methylene blue (C_o = 20 mg·L^{-1}).

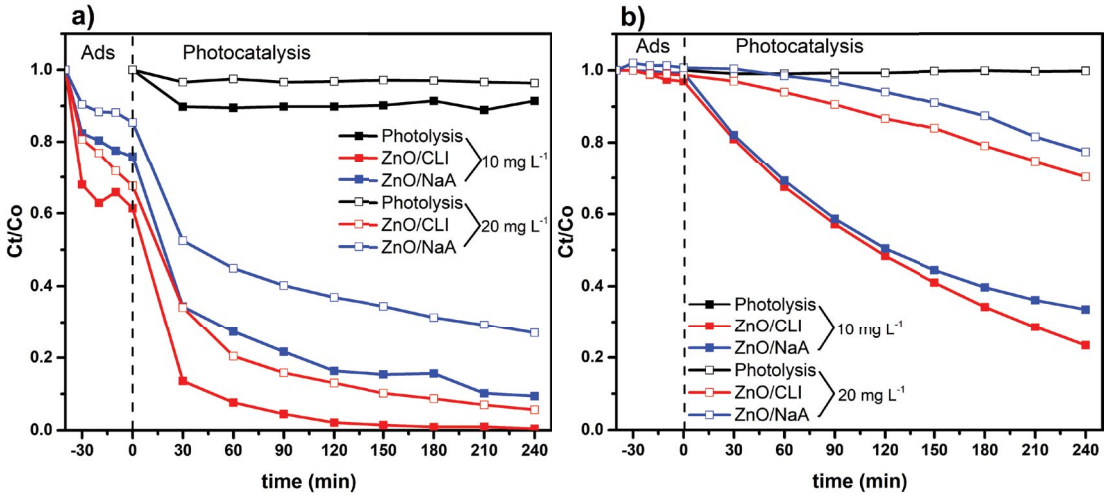

Fig. 8. Degradation efficiency of: (a) Methylene blue 10 and 20 mg·L^{-1} and (b) rhodamine B at 10 and 20 mg·L^{-1}.

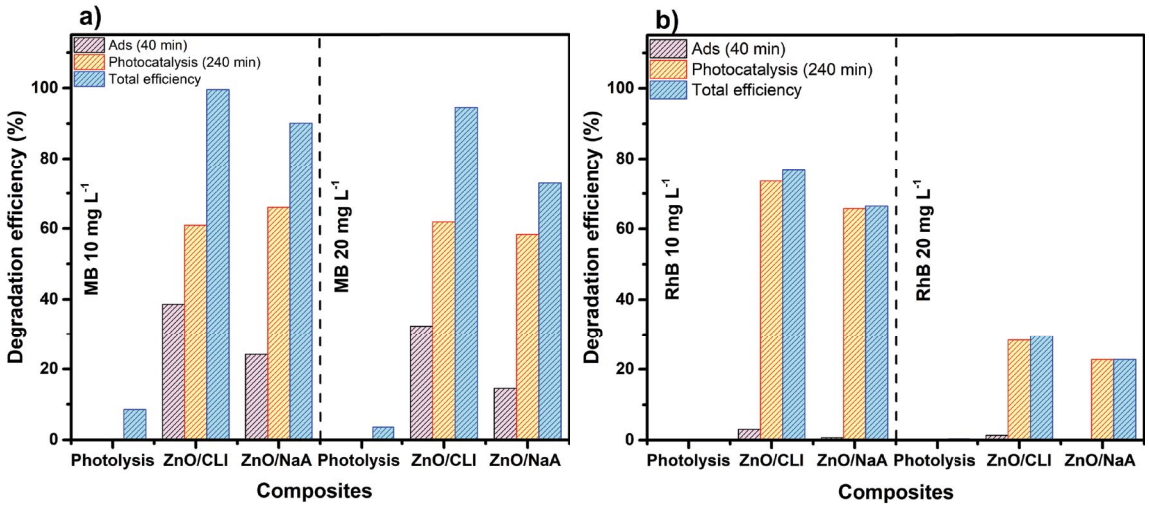

Fig. 9. Degradation efficiency of the compounds evaluated in (a) Methylene blue and (b) rhodamine B.

agglomeration of the ZnO particles and reduces the surface area [41,44].

3.8. Evaluation of the initial concentration of the dye

The photocatalytic activity of ZnO/CLI and ZnO/NaA of two concentrations of MB and RhB was evaluated. In Fig. 8a significant adsorption is observed for the composites in the dark time. In the first 30 min of UV irradiation, the MB concentration decreased, attributed to the area and adsorption in the dark time. On the other hand, the photocatalytic activity using RhB (Fig. 8b), adsorption is not observed in the dark time, however, when the solution is irradiated, the concentration decreases slowly, which is associated with the complexity of the molecule. It was determined that degradation efficiency was influenced by the concentration of the dyes. This is because both dyes are slowly eliminated when the concentration is increased, which is due to the saturation of the active sites of the photocatalyst.

Fig. 9 shows the percentages of degradation in the two stages of the evaluation (adsorption and photocatalysis). The ZnO/CLI composite showed higher degradation efficiency in both dyes at both concentrations, which is in agreement with the adsorption capacity of this natural zeolite and with the photocatalytic activity of pure ZnO.

4. Conclusion

ZnO, ZnO/CLI and ZnO/NaA photocatalysts were synthesized for the removal of organic dyes at low cost. The results showed that with low ZnO load and low photocatalyst load, it was possible to eliminate the contaminating dyes under study. The best photocatalytic efficiency was presented in the composite with natural zeolite (ZnO/CLI) due to its better adsorption capacity. The fact that a natural zeolite has shown better results compared to a synthetic zeolite is favorable for its production and implementation in larger-scale processes, since we have a natural resource available as a support for efficient photocatalysts.

Acknowledgments

Rojas-Blanco acknowledges for the support of CECYTET with the project PRODECTI-2022-01/56. Servín de Dios acknowledges CONACyT, Mexico, for financial support through the Master fellowship.

Conflicts of interest

The authors have no financial or proprietary interests in any material discussed in this article.

Symbols

% Deg	—	Degree of the photocatalytic degradation
C_0	—	Initial concentration
C_t	—	Concentration of dye at time t
τ	—	Average crystal size
k	—	Shape factor (0.9)
λ	—	Wavelength
θ	—	Position of the diffraction peak
β	—	Width at mean height of the diffraction peak
R	—	Absolute value of reflectance

References

[1] H. Xu, Q. Gao, B. Yuan, Analysis and identification of pollution sources of comprehensive river water quality: evidence from two river basins in China, Ecol. Indic., 135 (2022) 108561, doi: 10.1016/j.ecolind.2022.108561.

[2] S.H.S. Chan, T.Y. Wu, J.C. Juan, C.Y. Teh, Recent developments of metal oxide semiconductors as photocatalysts in advanced oxidation processes (AOPs) for treatment of dye wastewater, J. Chem. Technol. Biotechnol., 86 (2011) 1130–1158.

[3] E. Santoso, R. Ediati, Y. Kusumawati, H. Bahruji, D.O. Sulistiono, D. Prasetyoko, Review on recent advances of carbon-based adsorbent for methylene blue removal from wastewater, Mater. Today Chem., 16 (2020) 100233, doi: 10.1016/j.mtchem.2019.100233.

[4] S. Alvarez-Torrellas, M. Boutahala, N. Boukhalfa, M. Munoz, Effective adsorption of methylene blue dye onto magnetic nanocomposites. Modeling and reuse studies, Appl. Sci. (Switzerland), 9 (2019), doi: 10.3390/app9214563.

[5] G.M. Ziarani, R. Moradi, N. Lashgari, H.G. Kruger, Chapter 14 – Rhodamine Dyes, G.M. Ziarani, R. Moradi, N. Lashgari, H.G. Kruger, Eds., Metal-Free Synthetic Organic Dyes, Elsevier, 2018, pp. 185–191. Available at: https://doi.org/10.1016/b978-0-12-815647-6.00014-5

[6] E.E. Mbu, D. Dodoo-arhin, S.K. Ntwampe, E. Malenga, E. Fosso-kankeu, Photocatalytic Degradation of Azo and Rhodamine Dyes Using Copper(II) Oxide Nanoparticles, 10th Int'l Conference on Advances in Science, Engineering, Technology & Healthcare (ASETH-18) Nov. 19–20, Cape Town (South Africa), 2018. Available at: https://doi.org/10.17758/eares4.eap1118210

[7] W. Zheng, S. You, Y. Yao, L. Jin, Y. Liu, Development of atomic hydrogen-mediated electrocatalytic filtration system for peroxymonosulfate activation towards ultrafast degradation of emerging organic contaminants, Appl. Catal., B, 298 (2021) 120593, doi: 10.1016/j.apcatb.2021.120593.

[8] P.K. Rai, C. Sonne, R.J.C. Brown, S.A. Younis, K.-H. Kim, Adsorption of environmental contaminants on micro- and nano-scale plastic polymers and the influence of weathering processes on their adsorptive attributes, J. Hazard. Mater., 427 (2022) 127903, doi: 10.1016/j.jhazmat.2021.127903.

[9] A. Koubová, T. Van Nguyen, K. Grabicová, V. Burkina, F.G. Aydin, R. Grabic, P. Nováková, H. Švecová, P. Lepič, G. Fedorova, T. Randák, V. Žlábek, Metabolome adaptation and oxidative stress response of common carp (*Cyprinus carpio*) to altered water pollution levels, Environ. Pollut., 303 (2022) 119117, doi: 10.1016/j.envpol.2022.119117.

[10] Y. Zhao, Y. Wang, H. Chi, Y. Zhang, C. Sun, H. Wei, R. Li, Coupling photocatalytic water oxidation on decahedron $BiVO_4$ crystals with catalytic wet peroxide oxidation for removing organic pollutions in wastewater, Appl. Catal., B, 318 (2022) 121858, doi: 10.1016/j.apcatb.2022.121858.

[11] Y. Sun, D. Li, X. Lu, J. Sheng, X. Zheng, X. Xiao, Flocculation of combined contaminants of dye and heavy metal by nano-chitosan flocculants, J. Environ. Manage., 299 (2021) 113589, doi: 10.1016/j.jenvman.2021.113589.

[12] C. Liu, M. Zhang, H. Gao, L. Kong, S. Fan, L. Wang, H. Shao, M. Long, X. Guo, Cyclic coupling of photocatalysis and adsorption for completely safe removal of N-nitrosamines in water, Water Res., 209 (2022) 117904, doi: 10.1016/j.watres.2021.117904.

[13] H. Wang, Y. Yang, Z. Zhou, X. Li, J. Gao, R. Yu, J. Li, N. Wang, H. Chang, Photocatalysis-enhanced coagulation for removal of intracellular organic matter from *Microcystis aeruginosa*: efficiency and mechanism, Sep. Purif. Technol., 283 (2022) 120192, doi: 10.1016/j.seppur.2021.120192.

[14] A. Karami, R. Monsef, M.R. Shihan, L.Y. Qassem, M.W. Falah, M. Salavati-Niasari, UV-light-induced photocatalytic response

of Pechini sol–gel synthesized erbium vanadate nanostructures toward degradation of colored pollutants, Environ. Technol. Innovation, 28 (2022) 102947, doi: 10.1016/j.eti.2022.102947.
[15] L. Pan, Z. Wan, Q. Feng, J. Wang, J. Xiong, S. Wang, H. Zhu, G. Chen, Biofilm response and removal *via* the coupling of visible-light-driven photocatalysis and biodegradation in an environment of sulfamethoxazole and Cr(VI), J. Environ. Sci., 122 (2022) 50–61.
[16] A. Saravanan, P. Senthil Kumar, S. Jeevanantham, M. Anubha, S. Jayashree, Degradation of toxic agrochemicals and pharmaceutical pollutants: effective and alternative approaches toward photocatalysis, Environ. Pollut., 298 (2022) 118844, doi: 10.1016/j.envpol.2022.118844.
[17] M.P. Gonullu, Design and characterization of single bilayer ZnO/Al_2O_3 film by ultrasonically spray pyrolysis and its application in photocatalysis, Micro Nanostruct., 164 (2022) 107113, doi: 10.1016/j.spmi.2021.107113.
[18] P. Nandi, D. Das, ZnO/CdS/CuS heterostructure: a suitable candidate for applications in visible-light photocatalysis, J. Phys. Chem. Solids, 160 (2022) 110344, doi: 10.1016/j.jpcs.2021.110344.
[19] S.H. Park, T. Kim, A.N. Kadam, C. Bathula, A.A. Ghfar, H. Kim, S.-W. Lee, Synergistic photocatalysis of Z-scheme type Fe_2O_3/g-C_3N_4 heterojunction coupled with reduced graphene oxide, Surf. Interfaces, 30 (2022) 101910, doi: 10.1016/j.surfin.2022.101910.
[20] Q. Zhang, X. Zhao, L. Duan, H. Shen, R. Liu, Controlling oxygen vacancies and enhanced visible light photocatalysis of CeO_2/ZnO nanocomposites, J. Photochem. Photobiol., A, 392 (2020) 112156, doi: 10.1016/j.jphotochem.2019.112156.
[21] D. Xu, H. Ma, Degradation of rhodamine B in water by ultrasound-assisted TiO2 photocatalysis, J. Cleaner Prod., 313 (2021) 127758, doi: 10.1016/j.jclepro.2021.127758.
[22] Q. Gao, Z. Liu, $FeWO_4$ nanorods with excellent UV–visible light photocatalysis, Prog. Nat. Sci.: Mater. Int., 27 (2017) 556–560.
[23] A. Kumar, Mu. Naushad, A. Rana, Inamuddin, Preeti, G. Sharma, A.A. Ghfar, F.J. Stadler, M.R. Khan, ZnSe-WO_3 nano-hetero-assembly stacked on Gum ghatti for photo-degradative removal of Bisphenol A: symbiose of adsorption and photocatalysis, Int. J. Biol. Macromol., 104 (2017) 1172–1184.
[24] Z. Li, K. Dai, J. Zhang, C. Liang, G. Zhu, Facile synthesis of novel octahedral Cu_2O/Ag_3PO_4 composite with enhanced visible light photocatalysis, Mater. Lett., 206 (2017) 48–51.
[25] M. Salavati-Niasari, F. Davar, Z. Fereshteh, Synthesis and characterization of ZnO nanocrystals from thermolysis of new precursor, Chem. Eng. J., 146 (2009) 498–502.
[26] M. Nazarkovsky, B. Czech, A. Żmudka, V.M. Bogatyrov, O. Artiushenko, V. Zaitsev, T.D. Saint-Pierre, R.C. Rocha, J. Kai, Y. Xing, W.D.G. Gonçalves, A.G. Veiga, M.L.M. Rocco, S.H. Safeer, M.V. Galaburda, V. Carozo, R.Q. Aucélio, R.J. Caraballo-Vivas, O.I. Oranska, J. Dupont, Structural, optical and catalytic properties of ZnO-SiO_2 colored powders with the visible light-driven activity, J. Photochem. Photobiol., A, 421 (2021) 113532, doi: 10.1016/j.jphotochem.2021.113532.
[27] M.A. Wahba, S.M. Yakout, R. Khaled, Interface engineered efficient visible light photocatalytic activity of MWCNTs/Co doped ZnO nanocomposites: morphological, optical, electrical and magnetic properties, Opt. Mater. (Amst), 115 (2021) 111039, doi: 10.1016/j.optmat.2021.111039.
[28] M. Yousefi, F. Gholamian, D. Ghanbari, M. Salavati-Niasari, Polymeric nanocomposite materials: preparation and characterization of star-shaped PbS nanocrystals and their influence on the thermal stability of acrylonitrile–butadiene–styrene (ABS) copolymer, Polyhedron, 30 (2011) 1055–1060.
[29] R. Monsef, M. Ghiyasiyan-Arani, M. Salavati-Niasari, Design of magnetically recyclable ternary $Fe_2O_3/EuVO_4$/g-C_3N_4 nanocomposites for photocatalytic and electrochemical hydrogen storage, ACS Appl. Energy Mater., 4 (2021) 680–695.
[30] M. Salavati-Niasari, J. Hasanalian, H. Najafian, Alumina-supported $FeCl_3$, $MnCl_2$, $CoCl_2$, $NiCl_2$, $CuCl_2$, and $ZnCl_2$ as catalysts for the benzylation of benzene by benzyl chloride, J. Mol. Catal. A: Chem., 209 (2004) 209–214.
[31] D. Zhang, X. Zuo, W. Gao, H. Huang, H. Zhang, T. Cong, S. Yang, J. Zhang, L. Pan, Recyclable ZnO/Fe_3O_4 nanocomposite with piezotronic effect for high performance photocatalysis, Mater. Res. Bull., 148 (2022) 111677, doi: 10.1016/j.materresbull.2021.111677.
[32] S. Lu, Y. Ma, L. Zhao, Production of ZnO-CoO_x-CeO_2 nanocomposites and their dye removal performance from wastewater by adsorption-photocatalysis, J. Mol. Liq., 364 (2022) 119924, doi: 10.1016/j.molliq.2022.119924.
[33] X. Zhang, J. Peng, X. Qi, Y. Huang, J. Qiao, Y. Guo, X. Guo, Y. Wu, Nanocellulose/carbon dots hydrogel as superior intensifier of ZnO/AgBr nanocomposite with adsorption and photocatalysis synergy for Cr(VI) removal, Int. J. Biol. Macromol., 233 (2023) 123566, doi: 10.1016/j.ijbiomac.2023.123566.
[34] G. Hu, J. Yang, X. Duan, R. Farnood, C. Yang, J. Yang, W. Liu, Q. Liu, Recent developments and challenges in zeolite-based composite photocatalysts for environmental applications, Chem. Eng. J., 417 (2021) 129209, doi: 10.1016/j.cej.2021.129209.
[35] S. Behravesh, N. Mirghaffari, A.A. Alemrajabi, F. Davar, M. Soleimani, Photocatalytic degradation of acetaminophen and codeine medicines using a novel zeolite-supported TiO_2 and ZnO under UV and sunlight irradiation, Environ. Sci. Pollut. Res., 27 (2020) 26929–26942.
[36] M. Salavati-Niasari, Zeolite-encapsulation copper(II) complexes with 14-membered hexaaza macrocycles: synthesis, characterization and catalytic activity, J. Mol. Catal. A: Chem., 217 (2004) 87–92.
[37] N. Sobuś, I. Czekaj, Lactic acid conversion into acrylic acid and other products over natural and synthetic zeolite catalysts: theoretical and experimental studies, Catal. Today, 387 (2022) 172–185.
[38] J. Liu, Z. Huang, J. Sun, Y. Zou, B. Gong, Enhancing the removal performance of Cd(II) from aqueous solutions by NaA zeolite through doped thiourea reduced GO which is trapped within zeolite crystals, J. Alloys Compd., 815 (2020) 152514, doi: 10.1016/j.jallcom.2019.152514.
[39] J.R. Torres-Hernández, E. Ramírez-Morales, L. Rojas-Blanco, J. Pantoja-Enriquez, G. Oskam, F. Paraguay-Delgado, B. Escobar-Morales, M. Acosta-Alejandro, L.L. Díaz-Flores, G. Pérez-Hernández, Structural, optical and photocatalytic properties of ZnO nanoparticles modified with Cu, Mater. Sci. Semicond. Process., 37 (2015) 87–92.
[40] Y. Costa-Marrero, M. Andrade, J. Ellena, J. Duque-Rodríguez, T. Farias, G. Autié-Castro, Zeolite/ZnO composites based on a Cuban natural clinoptilolite and preliminary evaluation in methylene blue adsorption, Mater. Res. Express, 7 (2020) 015066, doi: 10.1088/2053-1591/ab6a5c.
[41] R. Mahdavi, S.S.A. Talesh, Sol–gel synthesis, structural and enhanced photocatalytic performance of Al doped ZnO nanoparticles, Adv. Powder Technol., 28 (2017) 1418–1425.
[42] E. Chmielewská, W. Tylus, M. Bujdoš, Study of mono- and bimetallic Fe and Mn oxide-supported clinoptilolite for improved Pb(II) removal, Molecules, 26 (2021) 4143, doi: 10.3390/molecules26144143.
[43] J. Cao, P. Wang, J. Shen, Q. Sun, Core-shell Fe_3O_4@zeolite NaA as an adsorbent for Cu^{2+}, Materials, 13 (2020, doi: 10.3390/ma13215047.
[44] P.L. da Silva, R.P. Nippes, P.D. Macruz, F.L. Hegeto, M.H.N.O. Scaliante, Photocatalytic degradation of hydroxychloroquine using ZnO supported on clinoptilolite zeolite, Water Sci. Technol., 84 (2021) 763–776.
[45] V.R. Batistela, L.Z. Fogaça, S.L. Fávaro, W. Caetano, N.R.C. Fernandes-Machado, N. Hioka, ZnO supported on zeolites: photocatalyst design, microporosity and properties, Colloids Surf., A, 513 (2017) 20–27.
[46] A. Khorsand Zak, W.H. Abd. Majid, M.E. Abrishami, R. Yousefi, X-ray analysis of ZnO nanoparticles by Williamson–Hall and size-strain plot methods, Solid State Sci., 13 (2011) 251–256.
[47] V. Mote, Y. Purushotham, B. Dole, Williamson–Hall analysis in estimation of lattice strain in nanometer-sized ZnO particles, J. Theor. Appl. Phys., 6 (2012) 2–9.
[48] V.R. Venu Gopal, S. Kamila, Effect of temperature on the morphology of ZnO nanoparticles: a comparative study, Appl. Nanosci., 7 (2017) 75–82.

[49] F. Alakhras, E. Alhajri, R. Haounati, H. Ouachtak, A.A. Addi, T.A. Saleh, A comparative study of photocatalytic degradation of rhodamine B using natural-based zeolite composites, Surf. Interfaces, 20 (2020) 100611, doi: 10.1016/j.surfin.2020.100611.
[50] R.P. Nippes, D. Frederichi, e M.H.N. Olsen Scaliante, Enhanced photocatalytic performance under solar radiation of ZnO through hetero-junction with iron functionalized zeolite, J. Photochem. Photobiol., A, 418 (2021) 113373, doi: 10.1016/j.jphotochem.2021.113373.
[51] A.A. Alswata, M. Bin Ahmad, N.M. Al-Hada, H.M. Kamari, M.Z. Bin Hussein, N.A. Ibrahim, Preparation of zeolite/zinc oxide nanocomposites for toxic metals removal from water, Results Phys., 7 (2017) 723–731.
[52] W. Lopes de Almeida, N.S. Ferreira, F.S. Rodembusch, V. Caldas de Sousa, Study of structural and optical properties of ZnO nanoparticles synthesized by an eco-friendly tapioca-assisted route, Mater. Chem. Phys., 258 (2021) 123926, doi: 10.1016/j.matchemphys.2020.123926.
[53] D.T. Hieu, H. Kosslick, M. Riaz, A. Schulz, A. Springer, M. Frank, C. Jaeger, N.T. Thu, L.T. Son, Acidity and stability of Brønsted acid sites in green clinoptilolite catalysts and catalytic performance in the etherification of glycerol, Catalysts, 12 (2022) 253, doi: 10.3390/catal12030253.
[54] O. Sacco, V. Vaiano, M. Matarangolo, ZnO supported on zeolite pellets as efficient catalytic system for the removal of caffeine by adsorption and photocatalysis, Sep. Purif. Technol., 193 (2018) 303–310.
[55] A. Shokrollahi, S. Sharifnia, Optimization of aqueous NH_4^+/NH_3 photodegradation by ZnO/zeolite y composites using response surface modeling, Int. J. Chem. Reactor Eng., 17 (2019), doi: 10.1515/ijcre-2018-0042.
[56] Y. Xu, H. Li, B. Sun, P. Qiao, L. Ren, G. Tian, B. Jiang, K. Pan, W. Zhou, Surface oxygen vacancy defect-promoted electron-hole separation for porous defective ZnO hexagonal plates and enhanced solar-driven photocatalytic performance, Chem. Eng. J., 379 (2020) 122295, doi: 10.1016/j.cej.2019.122295.
[57] E.T. Wahyuni, N.P. Diantariani, I. Kartini, A. Kuncaka, Enhancement of the photostability and visible photoactivity of ZnO photocatalyst used for reduction of Cr(VI) ions, Results Eng., 13 (2022) 100351, doi: 10.1016/j.rineng.2022.100351.
[58] H. Aysan, S. Edebali, C. Ozdemir, M. Celik Karakaya, N. Karakaya, Use of chabazite, a naturally abundant zeolite, for the investigation of the adsorption kinetics and mechanism of methylene blue dye, Microporous Mesoporous Mater., 235 (2016) 78–86.
[59] J.G. Piedra López, O.H. González Pichardo, J.A. Pinedo Escobar, D.A. de Haro del Río, H. Inchaurregui Méndez, L.M. González Rodríguez, Photocatalytic degradation of metoprolol in aqueous medium using a TiO_2/natural zeolite composite, Fuel, 284 (2021) 119030, doi: 10.1016/j.fuel.2020.119030.
[60] N.P. Diantariani, I. Kartini, A. Kuncaka, E.T. Wahyuni, ZnO incorporated on natural zeolite for photodegradation of methylene blue, Rasayan J. Chem., 13 (2020) 747–756.
[61] H. Li, W. Zhang, Y. Liu, HZSM-5 zeolite supported boron-doped TiO_2 for photocatalytic degradation of ofloxacin, J. Mater. Res. Technol., 9 (2020) 2557–2567.
[62] C.J. Li, Y.J. Zhang, H. Chen, P.Y. He, Y. Zhang, Q. Meng, Synthesis of fly ash cenospheres-based hollow ABW zeolite for dye removal via the coupling of adsorption and photocatalysis, Adv. Powder Technol., 32 (2021) 3436–3446.
[63] M. Bahrami, A. Nezamzadeh-Ejhieh, Effect of the supported ZnO on clinoptilolite nano-particles in the photodecolorization of semi-real sample bromothymol blue aqueous solution, Mater. Sci. Semicond. Process., 30 (2015) 275–284.
[64] Z. Heidari, R. Alizadeh, A. Ebadi, N. Oturan, M.A. Oturan, Efficient photocatalytic degradation of furosemide by a novel sonoprecipited ZnO over ion exchanged clinoptilolite nanorods, Sep. Purif. Technol., 242 (2020) 116800, doi: 10.1016/j.seppur.2020.116800.